ELSEVIER

Finite Element Simulations of Fiber Pullout Toughening in Fiber Reinforced Cement Based Composites

Cheng Yu Li* and Barzin Mobasher†
**Vaughn & Melton Consulting Engineers, Asheville, North Carolina, USA; and †Department of Civil and Environmental Engineering, Arizona State University, Tempe, Arizona, USA*

The role of fibers in fiber reinforced cement based composites was studied by means of finite element method. The study was conducted in two steps. The first step simulated the fiber pullout from a cementitious matrix and resulted in pullout force vs. slip displacement response. The pullout response was used in the second step as the bridging pressure applied over the crack length in composite specimen. The contribution of fiber's closing pressure was quantitatively measured through calculation of the J-integral and the effective stress intensity factor. The interfacial zone was characterized as a third phase with a lower stiffness and strength as compared to matrix and fiber. The debonding criterion was based on a yield surface defined by normal and shear strength of the interface. After debonding, Coulomb friction was introduced in the debonded zone. Effects of interfacial adhesional strength, clamping pressure, and fiber length on the fiber pullout response were studied. In the composite response simulations, the fibers across a prescribed crack length were modeled as nonlinear spring elements. The pullout force vs. slip displacement was used for the stiffness of the spring elements. J-integral was evaluated for the two cases of with and without fibers, and the difference between the two was used as the toughening contribution of fibers. The fiber toughening effect was studied for different fiber lengths and interface parameters. Results were compared with analytical simulations of crack growth using R-curves and a simplified approach based on linear crack opening–closing pressure relationship. Advanced Cement Based Materials 1998, 7, 123–132. *© 1998 Elsevier Science Ltd.*

KEY WORDS: Brittle matrix composites, Closing pressure, Composite materials, Fiber pullout, Fiber reinforced concrete, Finite element method, Fracture, Interfacial properties, J-integral, Steel fibers, Strength, Toughening, Toughness

Cement based materials are brittle in nature but show an increase in both ductility and strength with addition of fibers. The propagation of a crack is governed by the energy balance criteria defined when the applied stress intensity factor reaches the critical stress intensity factor. Crack growth may be arrested by strong fibers that are intersected along the crack propagation path. The unique mechanical properties of the interface between a fiber and bulk cement paste influence the strength, toughness, and durability of the composite material. Due to the interfacial failure, fibers are pulled out from the matrix and bridging forces are developed on the crack surfaces. The toughening component considered in the present work is due to the fiber bridging in the wake region. The bridging forces shield the crack and hence reduce the stress intensity factor at the crack tip. Interfacial shear strength plays a dominant role since the bridging pressure from fiber pullout is governed mainly by shear stress resistance between fibers and matrix. High levels of interfacial shear strength may prevent fibers from complete debonding and result in fiber fracture. Although the strength of the composite may increase, its toughness reduces significantly and failure is brittle. A low interfacial shear strength causes the fibers to debond easily, resulting in limited toughening contribution.

The toughness and strength of fiber reinforced composites are affected by the properties of fiber, matrix, and interface [1,2]. To compute the toughening magnitude, the bridging force distribution over the crack length is required. This distribution depends on the interaction of the debonding fibers with the matrix crack. Closed-form solutions of bridging force have been derived by Cox [3].

Hydration of cement grains near a nonreacting surface of a fiber results in formation of interface hydration products, which may be different from the CSH gel. Such differences are due to (1) accumulation of water and development of a higher water cement ratio, and (2) nucleation and growth of calcium hydroxide crystals at a preferred orientation. This unique microstructure extends up to about 50 μm from the fiber surface, allowing us to consider it as a one-dimensional (1-D)

Address correspondence to: Dr. B. Mobasher, Department of Civil and Environmental Engineering, Arizona State University, P.O. Box 875306, Tempe, Arizona 85287-5306.
Received March 10, 1997; Accepted October 29, 1997

ISSN 1065-7355/98/$19.00
PII S1065-7355(97)00087-4

Advn Cem Bas Mat
1998;7:123–132

layer. In addition to scanning electron microscopic (SEM) observations, the relatively high porosity and low strength of the interfacial zone also have been verified through microhardness tests [4]. Interfacial properties have been measured using fiber pullout and pushout tests by Naaman and Shah [5] and Li et al. [6]. Using a single fiber pullout test under slip-controlled closed loop, Li et al. used the pullout force vs. slip displacement response to calculate the stiffness and shear strength of the interfacial zone [7]. Interfacial toughness and frictional sliding resistance can be measured through curve fitting the theoretical predictions of micromechanical models [8]. The mechanisms of fiber pullout from brittle matrices have been studied by both strength and fracture mechanics based approaches [9–11]. In strength based models, debonding occurs when the shear stress reaches the shear strength of the interface. Marshall and Oliver [11] and Hsueh [12,13] used a constant shear stress τ along a debonded interface. A Coulomb-type friction law has been used to study the effects of residual and thermal stresses by Hutchinson and Jensen [14] and Dollar and Steif [15]. In the fracture mechanics approach, the interfacial toughness controls the propagation of debonding zone. Gao et al. [16] and Stang and Shah [9] proposed that debonding takes place when the energy release into the interface equals its resistance energy.

Finite element analysis has been used to simulate the fiber pullout and pushout tests by Ballarini et al. [17] and others [18]. Ballarini et al. carried out a 2-D finite element method (FEM) study using Coulomb friction law. In their simulations, the shear strength of the interface was defined by a Mohr–Coulomb yield criterion. The effect of interfacial friction and residual stress on the pullout vs. pushout response was studied. Mital and Chamis [18] performed a 3-D FEM simulation of fiber pushout using an elastic perfectly plastic constitutive response to study various interfacial bond conditions.

A coupled finite element study of fiber pullout and three-point bending specimens reinforced with aligned short fibers with a central crack is conducted. Interfacial debonding is based on a strength approach, whereas Coulomb friction is used in the debonded zone. The shear stress distribution along the fiber length and the fiber pullout force vs. slip response are obtained. In addition, effects of interfacial properties, residual stress at interface, and fiber parameters are studied. Nonlinear spring elements are used to model the fibers that bridge a crack in a three-point bending specimen. The element stiffness of spring elements is given by the fiber pullout obtained earlier. J-integral around the crack tip and crack opening profiles are evaluated and used to calculate the toughness contribution from fibers.

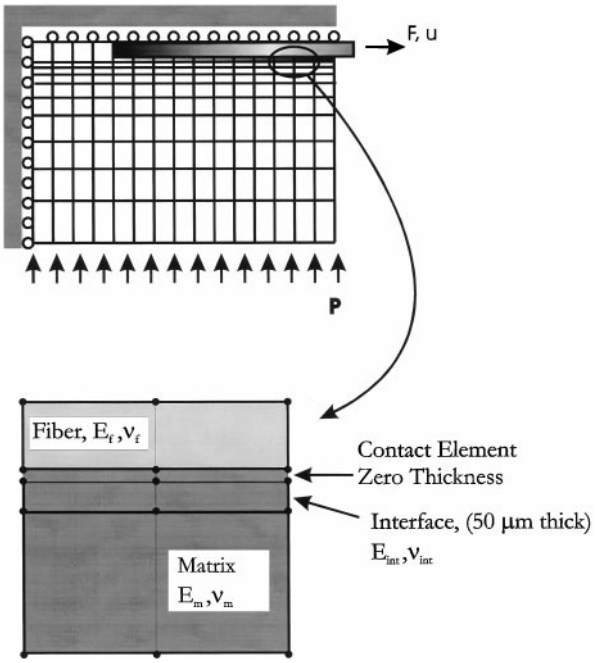

FIGURE 1. Schematic diagram of the finite element mesh for fiber pullout simulation.

Pullout Modeling

A 2-D axisymmetric finite element formulation was used to formulate the pullout of a single fiber from a cylindrical cementitious matrix. A linear elastic single fiber (E_f, ν_f), in a linear elastic cylindrical matrix (E_m, ν_m), was used. Four node axisymmetric plane strain elements were used for fiber, matrix, and interface. The interface was characterized as a linear elastic (E_{int}, ν_{int}) third phase with the thickness of 50 μm and the ratio of Young's modulus of the interface layer to the matrix phase of $E_{int}/E_m = 0.1$. A schematic representation of the finite element mesh is shown in Figure 1. A clamping pressure p was applied at the outer layer of matrix elements to simulate the effect of residual compressive stresses due to matrix shrinkage. This results in a normal stress distribution on the interface layer. Two sliding contact surfaces were defined, one on the elements representing the fiber and the other on the interface elements. The thickness of the contact elements was zero as they are initially bonded. As debonding occurs between these two contact surfaces, they may go through stages of debonding, slip, and/or separation during the fiber pullout process. After debonding, only the stress continuity across the sliding contact elements is preserved.

As compared to fiber and matrix phases, a lower strength and stiffness in the interface layer was implied. It is furthermore assumed that interface failure is governed by its yield surface as defined by the normal and shear strength. After the yield point, the interface

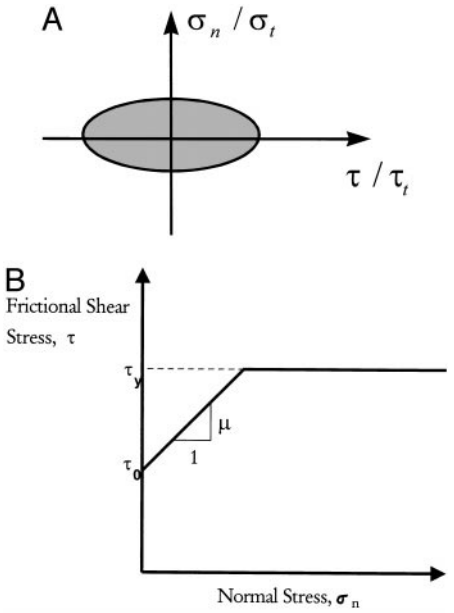

FIGURE 2. (A) Schematic diagram of the yield surface used for the debonding criteria of the fiber. (B) The Coulomb friction model for the debonded interface.

debonds and the shear stress is governed by Coulomb friction in the debonded zone. An isotropic debonding yield surface is expressed as a function of shear stress and the normal stress at the interface:

$$f = \sqrt{\left(\frac{\sigma_n}{\sigma_t}\right)^2 + \left(\frac{\tau}{\tau_t}\right)^2};\ (1 - f_{tol}) \le f \le (1 + f_{tol}) \qquad (1)$$

where σ_n, τ are the normal and shear stresses at the interface; σ_t, τ_t are the normal and shear strength of the interface; and f_{tol} is the tolerance in the numerical computations. The yield surface shown in Figure 2A is defined by eq. 1. In comparison to a Coulomb shear model, the present approach assumes a finite strength magnitude under high residual clamping stresses. By prescribing a relatively high compressive strength at the interface σ_t, contribution of the normal stress to the failure condition is reduced. In the limit case when σ_t increases to infinity, the solution converges to a constant shear strength criterion. A monotonic loading condition is used by incrementally increasing the imposed displacement at the fiber end and solving for the equilibrium. After debonding takes place for each element of the fiber, a Coulomb-type frictional traction was introduced at the contact surfaces of that element. Figure 2B shows the dependence of the frictional shear stress on the normal stress. The frictional shear stress has an initial value τ_0. It increases proportional to the normal stress up to a limiting value of τ_y as expressed in eq 2:

$$\tau_f = \tau_0 + \mu\sigma_n \le \tau_y \qquad (2)$$

where μ is the coefficient of friction between fiber and matrix as shown in Figure 2B. Note that the shear strength at the interface is directly proportional to the clamping pressure. Parameter τ_0 represents the frictional shear strength in the absence of normal stress. The second term in eq 2 takes into account the effect of normal stress σ_n in the debonded zone. Increasing the clamping pressure increases the shear strength. After the yield limit τ_y was reached, the Coulomb friction reduced to a constant-shear frictional model.

The loading is applied in two steps. Initially, the clamping pressure is applied along the outer layer of the mesh, and the elastic solution is obtained. The typical compressive pressures p applied was in the range of 5 to 9 MPa. The total displacement at the fiber end is prescribed next. The equilibrium solution is obtained by an incremental solution. The state of stress at the interface starts out in pure compression and, as the shear stress increases due to loading, the compressive stress at the interface decreases due to Poisson's contraction of the fiber. In order to govern the failure of the interface by means of a shear-type failure, a relatively high normal compressive strength σ_t of approximately 35 MPa was prescribed. This reduces the contribution of the normal stress to the failure condition and ensures that the yielding condition is governed by the shear criterion.

The nonlinear finite element code ABAQUS [19] was used. Unless otherwise specified, a constant friction coefficient of $\mu = 0.5$ and an initial normal stress $p = \sigma_n = 9$ MPa were used in the present approach. As discussed earlier, the normal strength σ_t was set equal to 35 MPa to ensure the shear strength failure. A ratio of Young's modulus of the interface layer to the matrix phase equal to 0.1 was used.

In order to ensure the stability of finite element solution during the various stages of fiber loading, a displacement-controlled algorithm was used. The total displacement at the fiber end was used as the limiting convergence criterion. This level of displacement was achieved in approximately 24 increments. After each incremental solution was obtained, load and slip at the fiber tip were obtained. The state of stress at the interface can be used to determine four conditions of elastic deformation, debonding, slipping, and/or opening. The pullout slip response of a fiber is shown in Figure 3A. The corresponding shear stress distribution during debonding stages 1 through 5 and the frictional pullout are shown in Figure 3B. The shear lag behavior and the termination of the elastic response at stage 2 are shown clearly in Figure 3B. Debonding is initiated by means of yielding at the interface and progresses from the loaded end. As the debonding propagates, the shear stresses at the embedded end continue to rise. Meanwhile, a constant shear stress due to the Coulomb-type

Advn Cem Bas Mat
1998;7:123–132

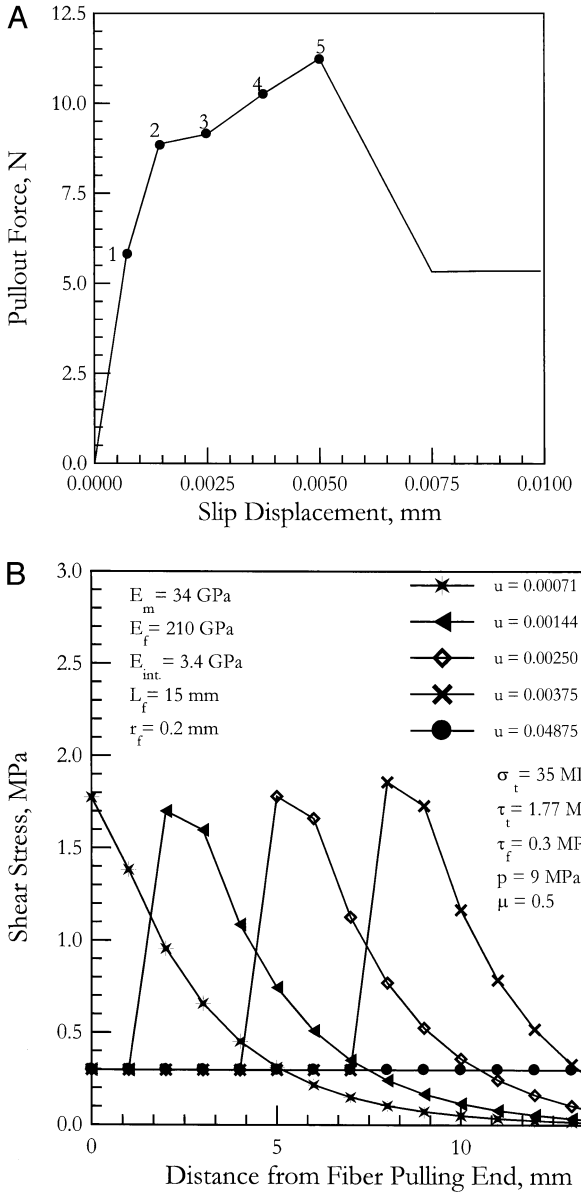

FIGURE 3. (A) Pullout force vs. slip response during various stages of fiber debonding. (B) Shear stress distribution along the fiber length during various stages of debonding.

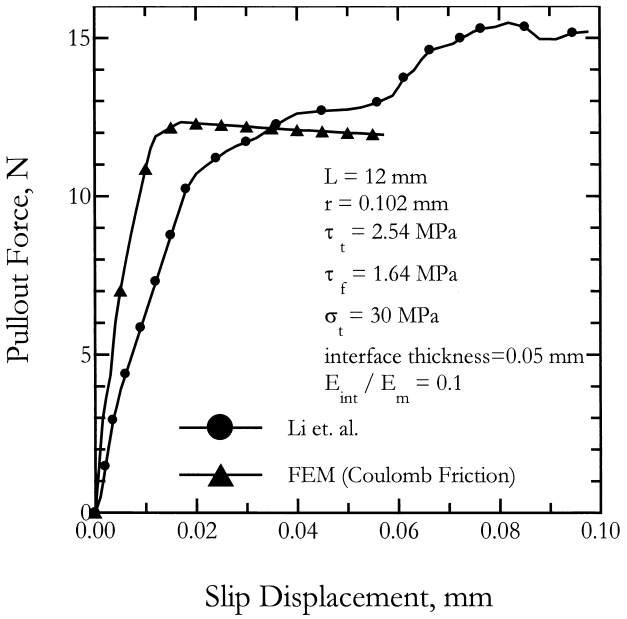

FIGURE 4. Comparison of the load vs. slip displacement for the FEM model with the experimental results.

constitutive model is applied at the debonded length. Stress distribution along the contact surface suggests that a debonding process that initially starts from the loaded end may, in later stages, switch to debonding at the embedded end. This process has been discussed in detail by Leung and Li [20]. The maximum load occurs under partial debonding conditions as shown by stage 4 in Figure 3B. Complete debonding is followed by the frictional pullout of the fiber, which is represented by a constant shear distribution and shown by a horizontal line in Figure 3B at the highest slip level.

Results of a pullout force vs. slip displacement curve are shown in Figure 4. The finite element simulation is in agreement with the experimental results obtained from Li et al. [7]. Note that the pullout force increases linearly up to 50% the peak load. Beyond this level, the response becomes nonlinear due to the propagation of the debonding zone. The peak load occurs under partial debonding conditions. This indicates that models that measure the interfacial characteristics by relating the ultimate load to the fiber embedded length may underestimate the shear stress. Furthermore, results of such a test would depend on the length of the fiber used. Although the present model fits the pullout strength reasonably well, the stiffness of the fiber pullout response is significantly overestimated using the FEM. Note that the prescribed shear stiffness of the interface was an order of magnitude lower than that of the cement based matrix.

Figure 5 represents the effect of increased adhesional bond strength on the pullout response. Note that by increasing the bond strength, the load carrying capacity and the stable debonding region of the interface increase significantly. By increasing the interfacial shear strength from 1.8 to 3.6 MPa, the maximum pullout force increases from 11.2 to 18.05 N, an increase of 61%. Increasing the interfacial shear strength increases the stiffness of the pullout force vs. slip displacement response. Figure 6 represents the effect of clamping pressure on the pullout response of the fibers. The load carrying capacity of the fiber increases proportional to the applied clamping pressure. This is due to the increase of the Coulomb friction and is more pro-

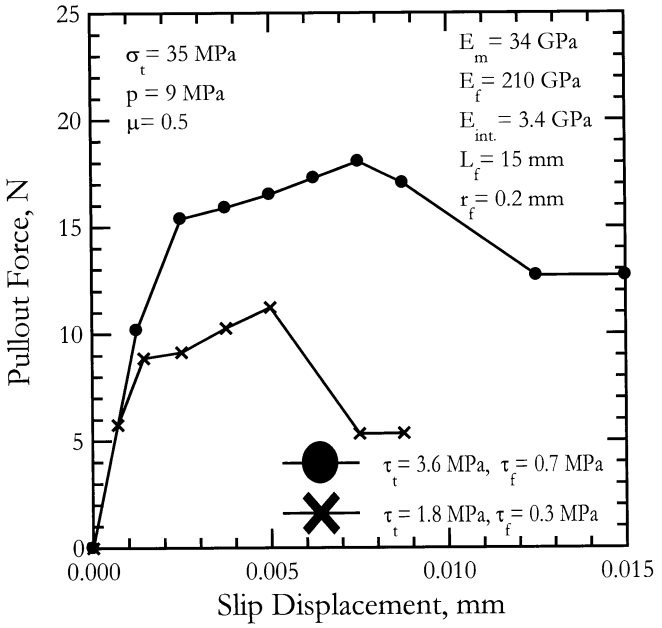

FIGURE 5. Effect of adhesional bond strength on the FEM pullout response.

nounced in the frictional pullout region of the response. In the post-peak region, the force drops steadily. This observation points out various anomalies observed in the interpretation of pullout test results. Many fiber pullout models attribute the sliding frictional pullout of the fiber to the shear strength of the interface with no regard to the effect of residual clamping pressures. This assumption results in computation of excessively high

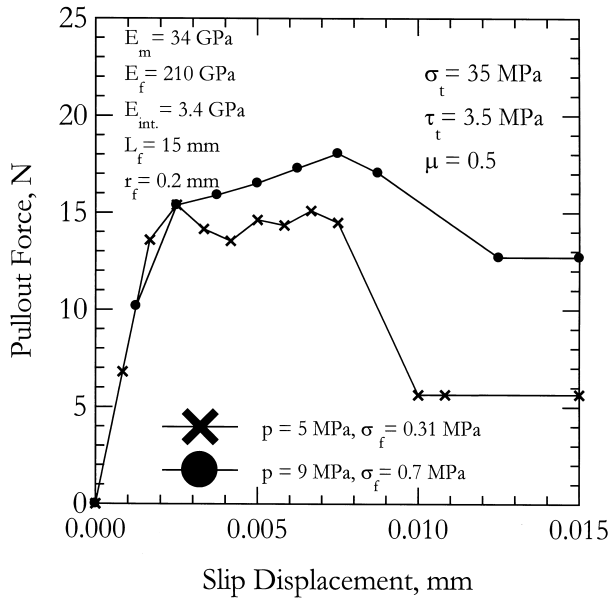

FIGURE 6. Effect of clamping pressure on the FEM pullout response.

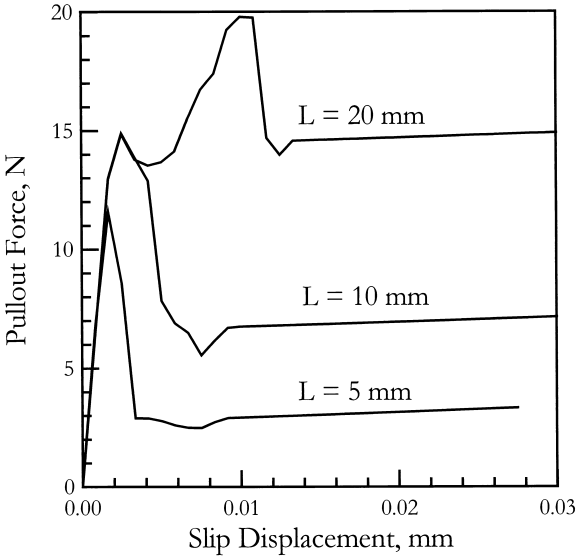

FIGURE 7. Effect of fiber length on the fiber pullout response.

shear strength values. In addition, various researchers have reported a relatively high coefficient of variation in these results. Hence, residual forces due to shrinkage may alter significantly the frictional nature of fiber pullout.

The effect of fiber length is shown in Figure 7. It shows that as the fiber length increases, the ultimate pullout force increases. It is shown that the initial stiffness is independent of the fiber length. Fiber debonding occurs at the same pullout force level, and the response becomes nonlinear thereafter. The load carrying capacity beyond this level increases as a function of the fiber length. After the interface completely debonds, pullout force drops to a constant frictional shear stress defined by the classical Coulomb friction law.

Fiber Toughening in Composites

In fiber reinforced composites, as the crack propagates and opens, bridging forces develop in the wake region due to the fiber pullout from the matrix. The toughness of the composite includes contributions from matrix and fibers. Using superposition, the stress intensity factor at the crack tip and crack opening displacement (COD) profile in the composite can be written as:

$$K_I^c = K_I^m + K_I^f \tag{3}$$

$$COD_c = COD_m + COD_f \tag{4}$$

where K_I^m and COD_m are the stress intensity factor and COD of a traction free crack due to applied forces, and

Advn Cem Bas Mat
1998;7:123–132

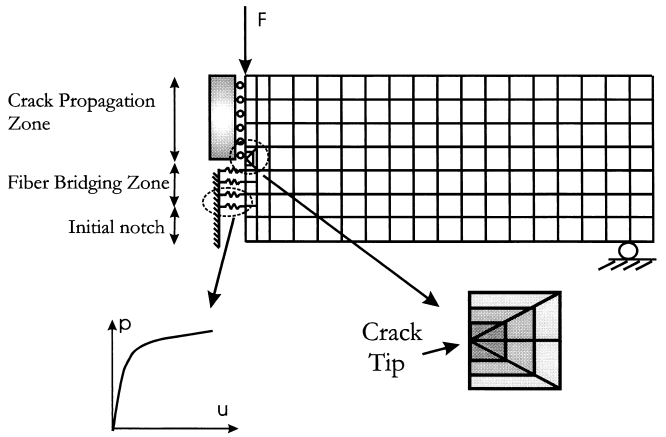

FIGURE 8. Schematic diagram of the FEM model for three-point bending specimen with a central crack and fibers in the bridging zone.

K_I^f and COD_f are the stress intensity factor and COD due to the bridging forces provided by fibers across the crack faces, which represent negative magnitudes. This superposition approach has been applied by Jenq and Shah [21], Ouyang and Shah [22], Hu and Mai [23], and others.

The difficulty of direct integration of eqs 3 and 4 is due to the dependence of distributed bridging force on the COD. Iterative procedures to solve these integral equations with a linear closing pressure term [24] or square root proportional to crack opening displacement [25] have been used. Jenq and Shah [21] modeled the bridge force as a softening response. The relationship between crack opening and bridging force also was studied by Mobasher and Li [26] using an R-curve approach. Instability conditions for the composite were defined using two parameters, critical stress intensity factor (K_{IC}) and critical crack tip opening displacement ($CTOD_c$). Using an iterative solution algorithm, the critical crack length and the corresponding load were obtained and used to construct the R-curve and the simulated load deformation of the composite. It was shown that crack opening profile depends on various stages of the crack growth.

In present simulations, the fiber contributions in eqs 3 and 4 are considered by introducing nonlinear spring elements that connect the nodes across the two faces of a crack. A schematic representation of the current model is shown in Figure 8. The stiffness of the spring elements is obtained from the fiber pullout response discussed in the previous section. Therefore, the effect of interface parameters is inherently incorporated in the closing pressure. By assuming uniform distribution of aligned fibers in the composite, the scale factor of the bridging force from single fiber pullout on each node can be determined as:

$$N = \frac{taV_f}{\pi r_f^2 (n-1)} \tag{5}$$

where t = specimen thickness; a = length of cracked ligament, V_f = volume fraction of fibers; r_f = fiber radius; and n = number of nodes defined on the cracked ligament [27]. For each finite element run, the crack length and applied load are prescribed. Due to the nonlinear nature of the problem, the load is increased incrementally to the prescribed level.

Finite Element Model for Composite

A three-point bending specimen with a central crack was studied using the finite element code ABAQUS. The specimen dimension was 25.4 × 76.2 × 330.2 mm and the initial crack length was 19 mm. The specimen dimensions were chosen to correspond to the experimental tests conducted earlier [27]. Due to the symmetry, only half of the beam was modeled, as shown in Figure 8. The beam material was linear elastic with Young's modulus and Poisson's ratio given by the rule of mixtures. A nonlinear geometry was assumed. Eight-node plane strain elements were used with 40 elements defined along the beam width direction and 30 elements in the span direction. The mesh was sufficiently refined around the crack tip to capture the tip singularity. This was verified by comparing the finite element results with the stress-intensity handbook values. Since the finite element code would not allow a negative stiffness definition for an element, only the ascending portion of the pullout response was used for the nonlinear spring elements. Further analysis confirmed that, for the cases studied, the half COD was indeed less than the fiber slip displacement at maximum pullout force. This indicates that for the cases studied in the present case, the fiber pullout region was not operative in the bridging zone. J-integral was evaluated through three independent paths defined around the crack tip, and the average of three values was used. Note that J-integral is independent of the integration path. The J-integral for a composite subjected to crack face traction by fiber pullout is defined as J_{eff} and represented by:

$$J_{eff} = \frac{K_I^{m^2}}{E'} + \int_0^{\delta_{tip}} \sigma(\delta) d\delta \tag{6}$$

where $E' = E$ for plane stress, and $E' = E/(1 - \upsilon^2)$ for plane strain conditions. In order to compute the two terms of this equation for a specific crack length, the analysis was conducted in two steps. In the first step, a specific crack extension was considered and the fiber bridging zone was invoked over the cracked ligament.

However, the fiber bridging zone was not included in the J-integral contours. Effect of crack face traction was treated by its superposition on the mechanical energy release rate. Definition of failure criteria for the matrix phase and considering the algebraic sign of the stress intensity factor due to the fiber, one may rewrite eq 6 as:

$$J_{eff} = \frac{K_I^{m^2}}{E'} - \int_0^{\delta_{tip}} \sigma(\delta) d\delta = \frac{K_I^c(F,\Delta a)^2}{E'} = \frac{K_{IC}{}^2}{E'}. \qquad (7)$$

An iterative procedure was conducted to compute the applied load such that the stress intensity factor at the tip of the crack $K_I^c(F,\Delta a)$ was equivalent to the plane strain fracture toughness of the matrix prescribed as K_{IC}. Due to the existence of fibers, a smaller crack opening was obtained, and a relatively high load was required to cause the effective stress intensity to be equal to the plane strain fracture toughness. Using this approach, the value of far-field load F was calculated by solving the nonlinear equation: $K_I^c(F,\Delta a) = K_{IC}$.

During the second stage of analysis, a specimen containing the same crack length without fibers in the bridging zone was studied. The same magnitude of load F obtained in the first stage of the analysis was applied. The value of J-integral corresponding to the linear elastic case as defined in eq 8 was obtained:

$$J_{LEFM} = \frac{K_I^m(F,\Delta a)^2}{E'}. \qquad (8)$$

Since the objective of the present research was to characterize the toughening effect of the fibers, the fiber reinforced composite material was assumed to be equivalent to a linear elastic material. Using the difference between the two J-values of eqs 7 and 8, an effective stress intensity factor measure in terms of an R-curve approach may be obtained using the following relationship:

$$K^R(a) = \sqrt{E' J_{LEFM}}. \qquad (9)$$

The difference between $K^R(a)$ and K_{IC} was defined as the contribution of the fibers. The finite element mesh size sensitivity was tested by comparing FEM based stress intensity factors for different crack lengths with the linear elastic fracture mechanics (LEFM) solutions by Tada et al. [28]. Results were within 1% of the values computed for a three-point bending specimen with a traction-free central crack subjected to a point force. The second step of calibration was based on computation of crack opening profiles due to fiber point loads. The COD of a strip specimen subjected to a unit force pair acting on the crack surfaces was compared with the FEM solutions for a three-point bending specimen.

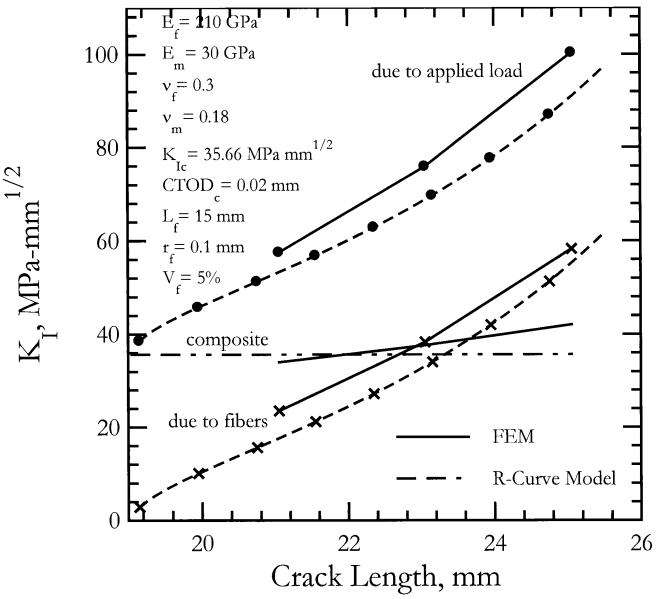

FIGURE 9. The stress intensity factor vs. crack length for a composite specimen reinforced with 5% steel fibers. The contribution of the fibers is shown as the crack growth takes place.

Results are discussed in detail elsewhere [27]. The COD profiles obtained from FEM were at most 3% larger than the LEFM based equations. This may be attributed to the finite length of the specimen used in FEM analysis and the rotation of the beam. The accuracy of the model was lower at the location of the point load. It was concluded that the present mesh is valid for the purposes of studying the stress intensity factor and crack opening profiles in the composite.

Analysis of Results

The stress intensity factor vs. crack length for a composite specimen reinforced with 5% steel fibers is shown in Figure 9. The analysis procedures are described as follows. Initially, the bridging elements across the cracked ligament are used, and the applied load was increased to obtain the stress intensity factor at the crack tip equal to the critical value for the matrix, prescribed as 35.66 MPa $mm^{1/2}$. The prescribed load was achieved by 40 increments in the simulations. The analysis was conducted for several crack sizes. In the second step of analysis, a traction free crack was used, and LEFM based J-integrals for the load levels obtained in the previous stage were calculated. Using the difference between these two cases, the contribution of fiber toughening component can be calculated. As shown in Figure 9, the fibers' contribution in reduction of the stress intensity factor increases as the crack propagates. As the crack length increases, the COD increases, re-

Advn Cem Bas Mat
1998;7:123–132

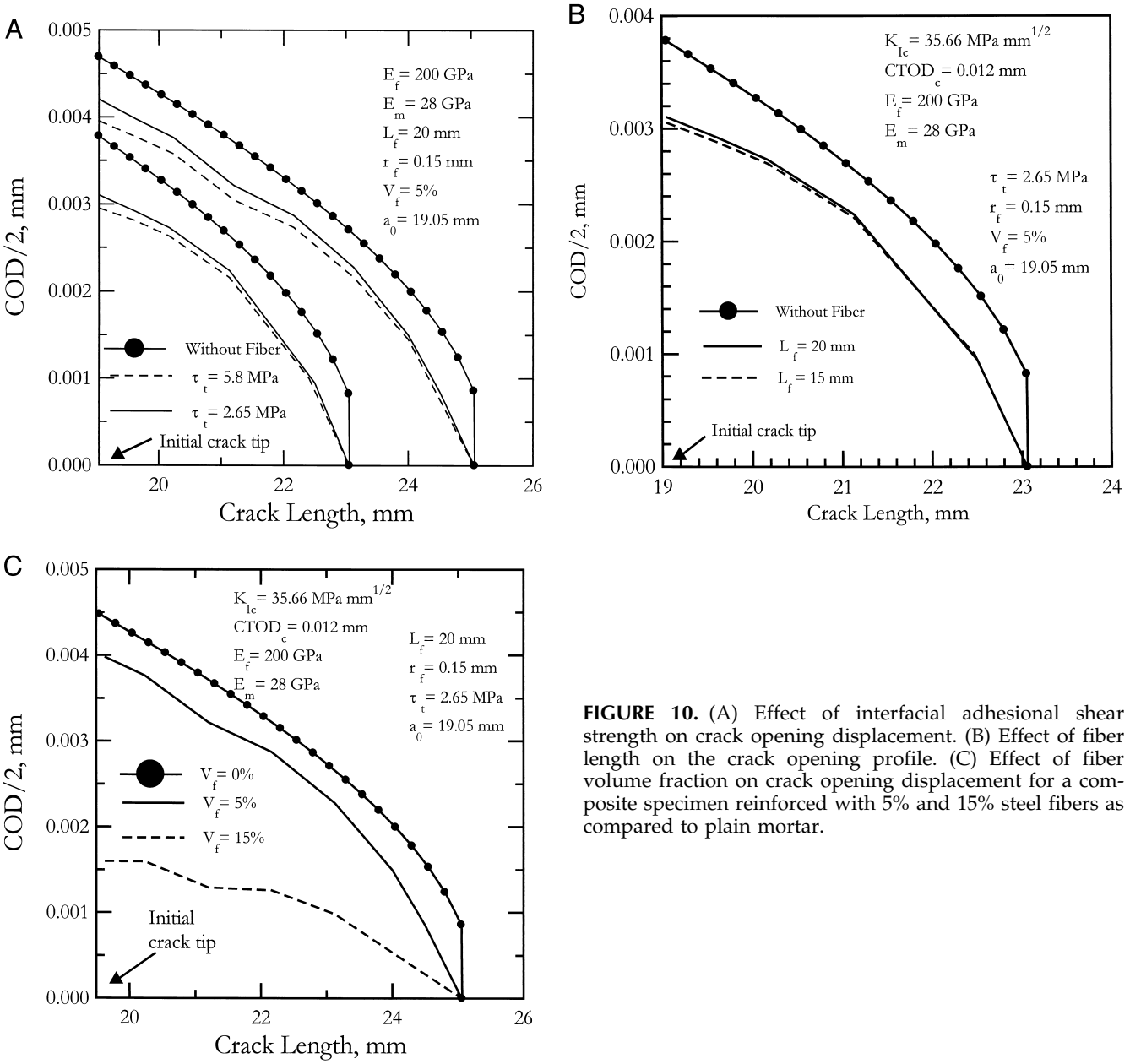

FIGURE 10. (A) Effect of interfacial adhesional shear strength on crack opening displacement. (B) Effect of fiber length on the crack opening profile. (C) Effect of fiber volume fraction on crack opening displacement for a composite specimen reinforced with 5% and 15% steel fibers as compared to plain mortar.

sulting in generation of a larger bridging force. The net effect of fibers is therefore in reduction of the stress intensity factor at the crack tip. At longer crack lengths, the major toughening contribution is from the fibers, i.e., at 5% fiber level, and crack extensions above 3 mm, the toughness of the composite is more than doubled as compared to the matrix phase. Results also are compared with the R-curve model by Mobasher and Li [26], which presents a numerical method for the solution of the problem. It can be seen that both approaches predict an increase of toughening contribution as crack propagation takes place; however, the FEM results are slightly higher than the R-curve model. Differences between the two models may be attributed to the failure criteria used. In the FEM model, a single failure criteria of stable crack growth at the critical stress intensity level is used. In the R-curve model, an additional criterion based on the critical COD was used.

Effects of interfacial adhesional strength, fiber length, and fiber volume fraction on the COD profiles are shown in Figures 10A, 10B, and 10C, respectively. No fibers were placed in the initial crack length, and only the COD profiles in the crack propagation region are presented. Figure 10A shows COD profiles at two crack lengths, indicating that increasing interfacial shear strength decreases the COD and, hence, the stress

intensity factor. As the interfacial shear strength increases, the stiffness of the pullout curve increases and fibers provide a higher bridging force at the same crack opening level. For the crack lengths studied, increasing the fiber length at the same volume fraction of fibers does not affect the COD, as shown in Figure 10B. It may be observed that the elastic stiffness of the fiber pullout force vs. slip response does not change appreciably with fiber length. As long as the crack opening level is in the elastic linear part of the pullout response, the effect of fiber length on the bridging force, hence the COD profiles, is not significant. As the fiber length increases, the debonding length may extend to a longer length, thus increasing the load carrying capacity of the fiber. The fiber length would then affect the toughness of the composite.

The number of fibers bridging the crack on each node was defined by eq 7. The bridging force increases proportional to the fiber fraction, resulting in a decrease in COD profiles. Figure 10C shows that COD at the tip of initial crack length reduces 50% with 5% fibers and 100% with 15% fibers at the 25-mm crack level.

Analysis of Toughening by a Simplified Procedure

For the cases studied, it may be shown that a simplified procedure may be used to compare the various methods used in the analysis. The component needed for such analysis is mainly the stiffness of fiber pullout region. In the present case, a stiffness of steel fiber in the ascending range obtained from finite element pullout simulation was used. The process involves approximate computation of the toughening term represented as:

$$\Delta J^* = \int_0^{\delta_{tip}} \sigma(\delta) d\delta. \tag{10}$$

Two cases of crack length of crack extensions of 4 and 6 mm corresponding to crack lengths of 23 and 25 mm are considered. The pullout scale factor $\Phi = V_f/\pi r^2 = 1.59$ is obtained for $V_f = 5\%$ and $r = 0.1$ mm. By assuming a linear relationship between the pullout load and the crack opening profile, a pullout stiffness value equivalent to $k = 3530$ N/mm is obtained from Figure 7. The expression of eq 10 may be reduced to: $\Delta J = 0.25 * k * \Phi * \delta_{tip}^2$. By using values of 0.0063 and 0.0085 mm as the crack tip opening displacements corresponding to two crack lengths of 23 and 25 mm, one would obtain an equivalent toughening component of 40.86 and 55.15 MPa $mm^{1/2}$. These values correspond quite well with the toughening values of 40 and 58 MPa $mm^{1/2}$ obtained from the FEM, as shown in Figure 9.

An alternative approach is to use the stress intensity factor reduction contributed by the bridging forces of the fibers across the crack face. This expression may be expressed as:

$$K_{Fiber} = \int_0^a \varphi P^* \left(\frac{COD(x)}{2} \right) g\left(1, \frac{x}{a}\right) dx \tag{11}$$

where function g(1, x/a) represents the function computing the stress intensity factor due to a unit load applied on the crack surface. The expressions for this function are provided in Mobasher and Li [26]. It was assumed that the crack opening profile is linear. An FEM based COD = 0.00425 mm corresponding to a composite containing 5% volume fraction of fibers was used from the model discussed in Figure 10A. It was assumed that this crack opening profile is linear, and the stiffness of the fiber pullout response was used to relate the crack opening to the closing pressure. For the crack of length 25 mm, a linear expression for the closing pressure as a function of position along may be expressed as $p = -2.5x + 62.5$ N (19 mm $< x <$ 25 mm). Parameter x represents the position in millimeters along crack length measured from the specimen surface. Substitution of this parameter in eq 11 and numerical integration of the resulting function results in stress intensity factor reduction due to the fibers of 30 and 47.8 MPa $mm^{1/2}$. These values are approximately 30% and 17% less than the finite element values discussed earlier. Note that the linearization procedure for the crack opening profiles significantly underestimates the crack opening and thus the closing pressures. Furthermore, the linearization of the nonlinear pullout slip response underestimates the pullout force for a given crack opening. The combination of these two effects results in the differences observed. However, the simplified procedure provides an easy method to use the interface property, such as its stiffness, in the quantitative estimation of toughening in fiber reinforced composite materials.

Conclusions

An FEM for the fiber pullout problem is presented. The failure condition of the interface was modeled using a biaxial yield surface. After debonding, a Coulomb-type frictional force was applied at the debonded interface. Using this approach, the stable debonding process in the fiber was simulated. A yield surface based on interfacial normal and shear strength was used to describe the interfacial debonding. It is shown that the maximum pullout force occurs under partial interfacial debonding. The results of shear stress distribution along the fiber indicate that the debonding process initially starts from the loaded end. The effects of

parameters such as interfacial shear strength, residual stress, and fiber length on the fiber pullout response were studied. The resultant pullout force vs. slip displacement response was used as closing pressure across the main crack in the three-point bending specimens. The toughening effect of fibers was measured in terms of interfacial shear strength, stiffness, and composite properties such as fiber dimensions and volume fraction. Results indicate that the stiffness of the interfacial region plays a dominant role in the crack propagation response of the composite. Results of this study are in good agreement with R-curve models and models based on linear closing pressure distributions.

Acknowledgments

This study was conducted with financial support from National Science Foundation Research Initiation Award # MSM-9211063, program director Dr. Ken Chong. This support is greatly appreciated.

References

1. McCartney, L.N. *Proc. R. Soc. Lond.* **1987,** *A409*, 329–350.
2. Budiansky, B.; Hutchinson, J.W.; Evans, A.G. *J. Mech. Phys. Solids* **1986,** *343*, 167–189.
3. Cox, B.N. *Mech. Mater.* **1993,** *15*, 87–98.
4. Bentur, A.; Diamond, S.; Mindess, S. *J. Mater. Sci.* **1985,** *20*, 3610–3620.
5. Naaman, A.E.; Shah, S.P. *ASCE J. Struct. Div.* **1976,** *102*, 1537–1548.
6. Li, V.C.; Wang, Y.; Backer, S. *J. Compos.* **1990,** *21*, 132–140.
7. Li, Z.; Mobasher, B.; Shah, S.P. *J. Amer. Ceram. Soc.* **1991,** *74*, 2156–2164.
8. Mobasher, B.; Li, C.Y. *Compos. Engin.* **1995,** *5*, 1349–1365.
9. Stang, H.; Shah, S.P. *J. Mater. Sci.* **1986,** *21*, 953–957.
10. Naaman, A.E.; Namur, G.G.; Alwan, J.M.; Najm, H.S. *J. Struct. Engin.* **1991,** *117*, 2769–2800.
11. Marshall, D.B.; Oliver, W.C. *J. Amer. Ceram. Soc.* **1987,** *70*, 542–548.
12. Hsueh, C.H. *J. Mater. Sci.* **1990a,** *25*, 818–828.
13. Hsueh, C.H. *Mater. Sci. Engin.* **1990b,** *A123*, 1–11.
14. Hutchinson, J.W.; Jensen, H.M. *Mechan. Mater.* **1990,** *9*, 139–163.
15. Dollar, A.; Steif, P.S. *Internat. J. Solids Struct.* **1993,** *30*, 1313–1329.
16. Gao, Y.C.; Mai, Y.W.; Cotterell, B. *J. Appl. Math Phys.* **1988,** *39*, 550–572.
17. Ballarini, R.; Ahmed, S.; Mullen, R.L. In *Proceedings of the International Conference on Interfaces in Metal Ceramics Composites, February 18–22*; 1990; pp 349–388.
18. Mital, S.K.; Chamis, C.C. *J. Compos. Technol. Res.* **1990,** *13*, 14–21.
19. *ABAQUS User's Manual Version 5.3*; Hibbitt, Karlsson, and Sorenson, Inc.: Providence, RI.
20. Leung, C.K.Y.; Li, V.C. *J. Mater. Sci.* **1991,** *26*, 5996–6010.
21. Jenq, Y.S.; Shah, S.P. *ASCE J. Struct. Engin.* **1986,** *112*, 19–34.
22. Ouyang, C.; Shah, S.P. *J. Amer. Ceram. Soc.* **1991,** *74*, 2831–2836.
23. Hu, X.Z.; Mai, Y.W. *Appl. Mech. Rev.* **1992,** *45*, 346–354.
24. Ouyang, C.; Shah, S.P. *Cem. Concr. Res.* **1992,** *22*, 1201–1215.
25. Marshall, D.B.; Cox, B.N.; Evans, A.G. *Acta Metal. Mater.* **1985,** *33*, 2013–2021.
26. Mobasher, B.; Li, C.Y. *Adv. Cem. Based Mater.* **1996,** *4*, 93–105.
27. Li, C.Y. *Ph.D. Dissertation*. Arizona State University, May 1995.
28. Tada, H.; Paris, P.C.; Irwin, G.R. *The Stress Analysis of Cracks Handbook*; Paris Production: St. Louis, 1985.